Load Characterization in High-Frequency IPT Systems Using Class EF Switching Waveforms

Juan M. Arteaga, *Member, IEEE*, Nunzio Pucci, Lingxin Lan, and Paul D. Mitcheson, *Senior Member, IEEE*

***Abstract*—Large magnetic field volumes associated with coreless high-frequency inductive power transfer (HF-IPT) systems allow multiple receivers to be powered from one transmitter, but also provide greater probability for foreign objects to couple to the system. Knowledge of the types of objects (legitimate receivers or otherwise) that are coupled to the transmitter is critical. Such knowledge on the transmit side would allow the system to be deactivated in the presence of foreign objects, and to determine the exact state of tuning of the receivers so that it may adjust itself accordingly to optimize system performance. This article introduces a technique to calculate the induced voltage generated by coupled receivers and foreign objects on the transmit coil in real time. Changes in the position or electrical quantities of the receivers, and foreign objects, alter the induced voltage on the transmit coil, and with it the trajectory of the switching waveforms of the inverter driving the transmit coil. From the shape of these waveforms, information on the phase and amplitude of the induced voltage can be extracted, thus enabling the induced voltage on the primary to be estimated with a single, easy to access, voltage measurement, which is easier than estimating the induced voltage from measurements of coil current and total coil voltage. We used a support-vector-machine (SVM) to perform regression analysis on the drain voltage data. The experimental setup uses a 100 W, 13.56 MHz Class EF inverter, and the model was generated from a large number of samples of the drain voltage waveforms operating at different known loads. These were generated from our in-house HF-IPT test load, which uses a Class EF synchronous rectifier. The results allow the induced voltage on the transmit coil to be estimated in real time from the drain voltage waveform alone, with a normalized root mean square error of 1.1% for the real part (reflected resistance) and 1.2% for the imaginary part (reflected reactance). This article is accompanied by a video file demonstrating the experiments.**

***Index Terms*—Impedance measurement, inductive power transmission, mutual coupling, resonant inverters.**

I. Introduction

Driving inductive power transfer (IPT) systems in the megahertz range, and specifically in the first three ISM bands (6.78, 13.56, and 27.12 MHz) exploits the possibility of high Q factors (>500), and consequently high efficiencies to be achieved at low coupling with compact and lightweight air-core coils.

High-frequency inductive power transfer (HF-IPT) systems tend to be designed with a wireless link comprised of air-core coils, since, as the frequency is increased, lower inductance coils can achieve the designed coil reactance. The physical limitations of the technology in terms of lowering the minimum useful value of coupling and increasing the power throughput are exemplified in the literature of the last 15 years. Most notably: in [1], a four coil-diameter transmit-to-receive separation was achieved; in [2], a multicoil dominoresonator was described, and in [3] an efficiency of over 70% with power levels higher than 50 W was achieved at a coupling factor lower than 4%. The most recent improvements to the technology are showcased by HF-IPT systems, which achieve over 80% efficiencies [4]–[8] and are retrofitted for applications [9]–[13]. These systems implement state-of-the-art megahertz power electronics designs at both ends of the system (e.g., [14]–[20]), allowing high efficiency to be achieved independent of large changes in load and large changes in the induced voltage on the receive coil.

Ferrite-based IPT systems are designed to shape the magnetic flux depending on the application. For example, in dynamic electric vehicle charging the shape of the flux is designed to maintain efficient operation while dealing with changes in horizontal alignment [21]–[24]. Conversely, air-core coil systems tend to have an uncontained magnetic flux shaped solely by the geometry of the electric conductor. This uncontained magnetic flux feature of HF-IPT systems with air-core coils is attractive for applications in which multiple receivers with different power requirements can be concurrently coupled to a transmitter. However, this does create a challenge for system operation as the receivers might be tuned slightly differently or, be embedded in equipment which has metallic frames or shields, which changes the link electromagnetic characteristics. Also, a large energized zone that allows multiple transmitters and receivers also increases the probability of presence of foreign objects, which in some applications is a major concern [25]. Measuring the induced voltage on the coils generated by a mutually coupled object (as for example done indirectly with auxiliary measurement coils [26]) can be a cost-effective solution to identify and monitor different loads and metallic objects

Manuscript received November 13, 2020; revised January 22, 2021 and March 5, 2021; accepted April 16, 2021. Date of publication April 21, 2021; date of current version June 30, 2021. This work was supported in part by the EPSRC Converter Architectures under Grant EP/R004137/1, in part by EPSRC Quietening Ultra-Low-Loss SiC, and GaN Waveforms under Grant EP/R029504/1, in part by EPSRC Impact Acceleration Account—Imperial College London 2020 under Grant EP/R511547/1, in part by SitS NSF-UKRI: Wireless In-Situ Soil Sensing Network for Future Sustainable Agriculture, under Grant NE/T011467/1, in part by the Department of Electrical and Electronic Engineering, Imperial College London, and in part by the University of Costa Rica. *(Juan M. Arteaga and Nunzio Pucci contributed equally to this work.)* Recommended for publication by Associate Editor D. G. Xu. *(Corresponding author: Juan M. Arteaga.)*

The authors are with the Department of Electrical, and Electronic Engineering, Imperial College London, London SW7 2AZ, U.K. (e-mail: j.arteaga-saenz15@imperial.ac.uk; nunzio.pucci15@imperial.ac.uk; lingxin.lan14@imperial.ac.uk; paul.mitcheson@imperial.ac.uk).

This article has supplementary material provided by the authors and color versions of one or more figures available at https://doi.org/10.1109/TPEL.2021.3074751.

Digital Object Identifier 10.1109/TPEL.2021.3074751

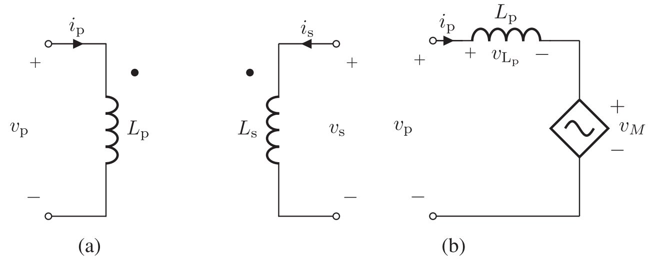

Fig. 1. Circuit diagrams of inductively coupled ideal coils. (a) Two-port representation of the link. (b) Equivalent circuit of the primary coil.

in real time without requiring additional sensors such as cameras, which can be expensive and significantly increase the cost and complexity of the system.

In this article, we use power converters with the Class EF topology [27], which have a single low-side switch and an output network of three capacitances and two inductances (one being the coil inductance), for the inverter and the synchronous rectifier, and we use, solely, the drain-voltage waveforms of the inverter to estimate the voltage induced by the receiver.

This article is organized as follows. Section II gives a theoretical overview of the system, highlighting on the challenges and complexities of measuring the induced voltage on the transmit coil produced by a coupled object. Section III gives an overview of the Class EF inverter topology, focusing on the range of loads that it can tolerate. Section IV describes the experimental setup to characterize the inverter switching waveforms with respect to the induced voltage by a controlled load. It then introduces candidate models to predict the phase and amplitude of the induced voltage by a mutually coupled object. Finally, results with passive loads are analyzed, illustrating a possible application of the technique and presenting the conclusion in Section V.

This article expands on our previous works [28]–[30] published as IEEE Conference Proceedings.

II. MEASURING THE INDUCED VOLTAGE OF A HF-IPT COIL UNDER TEST

An IPT link with air-core coils operating at a single frequency can be modeled as two ideal coupled inductors, each with a resistance in series to take into account the conduction losses in each coil. Using more complicated models, which include additional components is not necessary since the analysis can be focused at a single frequency, therefore allowing any model to be reduced to an impedance, quantified as complex number. This is applicable in HF-IPT systems since these operate in the ISM bands at a fixed frequency, or a very narrow band. In addition, since the coils operate at least close to resonance, and with relatively high loaded Q factors (typically higher than 10), the current is predominantly at the frequency of operation.

The voltage between the terminals of an ideal inductor with a self-inductance L_p, coupled with another ideal inductor with a self-inductance L_s, following the sign convention and the polarity of the mutual voltage of Fig. 1(a) is

$$v_\mathrm{p} = L_\mathrm{p}\frac{\mathrm{d}i_\mathrm{p}}{\mathrm{d}t} + M_\mathrm{ps}\frac{\mathrm{d}i_\mathrm{s}}{\mathrm{d}t} \tag{1}$$

where i_p and i_s are the currents in the primary and secondary circuits, respectively, and M_ps is the mutual inductance between L_p and L_s. The induced voltage produced by the secondary circuit ($v_\mathrm{M} = M_\mathrm{ps}\mathrm{d}i_\mathrm{s}/\mathrm{d}t$) can be represented as a dependent voltage source [see Fig. 1(b)], where in phasor notation[1] v_M can be expressed as

$$\boldsymbol{v_\mathrm{M}} = 2\pi f_{i_\mathrm{p}} k_\mathrm{ps}\sqrt{L_\mathrm{p}L_\mathrm{s}}\, i_\mathrm{s}\ \underline{/\theta_\mathrm{s} + 90^\circ}. \tag{2}$$

f_{i_p} is the frequency of the current in the primary coil [same as in the secondary (f_{i_s})], k_ps is the coupling factor, and θ_s is the phase of the current in the secondary coil. It should be noted that changing the polarity of the link introduces a 180° phase shift to θ_s, and consequently to $\boldsymbol{v_\mathrm{M}}$.

Traditionally, on the transmit side, the load of an IPT system is modeled as a resistance in series with the inductance of the transmit coil. This representation assumes a secondary circuit at resonance, where the reflected impedance $\boldsymbol{Z_\mathrm{eq}}$(), which is defined as

$$\boldsymbol{Z_\mathrm{eq}} = \frac{\boldsymbol{v_\mathrm{M}}}{\boldsymbol{i_\mathrm{p}}} \tag{3}$$

is real (R_eq), because $\boldsymbol{v_\mathrm{M}}$ is in phase with $\boldsymbol{i_\mathrm{p}}$ [see Fig. 1(b)]. This corresponds to the case in which $\theta_\mathrm{s} = -90^\circ$ with respect to the phase of $\boldsymbol{i_\mathrm{p}}$, ($\theta_\mathrm{p}$), and therefore, from (2)

$$\boldsymbol{v_\mathrm{M}}\Big|_{\theta_\mathrm{s}-\theta_\mathrm{p}=-90} = 2\pi f_{i_\mathrm{p}} k_\mathrm{ps}\sqrt{L_\mathrm{p}L_\mathrm{s}}\, i_\mathrm{s} \tag{4}$$

and from (3)

$$R_\mathrm{eq} = \boldsymbol{Z_\mathrm{eq}}\Big|_{\theta_\mathrm{s}-\theta_\mathrm{p}=-90} = \frac{2\pi f_{i_\mathrm{p}} k_\mathrm{ps}\sqrt{L_\mathrm{p}L_\mathrm{s}}\, i_\mathrm{s}}{i_\mathrm{p}}. \tag{5}$$

In this article, we model the influence of the receiver on the transmitter as a voltage source $\boldsymbol{v_\mathrm{M}}$ [see Fig. 1(b)] rather than an impedance. This allows the inverter's performance to be assessed independent of the amplitude and phase of $\boldsymbol{i_\mathrm{p}}$: for inductively coupled circuits that can be modeled as linear passive circuits (e.g., an *RLC* circuit) i_s is linearly dependent on i_p, and therefore the reflected impedance (at a fixed frequency and coupling) is constant. However, if i_s can be controlled with an active circuit i_s, and consequently v_M (2), are independent of i_p. Analyzing an inverter's performance with respect to the induced voltage on the IPT coil is useful not only for cases in which the reflected impedance is constant, but also when an active circuit such as another inverter or a synchronous rectifier is driving the secondary coil. Hence, it makes sense to model the effects of a secondary circuit as a voltage source rather than an impedance.

A. Considerations of Mismatch in Frequency and Harmonic Distortion

The representation of v_M as a phasor (2) assumes that i_p and i_s have the same frequency. Therefore, if both coils are driven

---

[1] Complex phasor quantities are marked as bold.

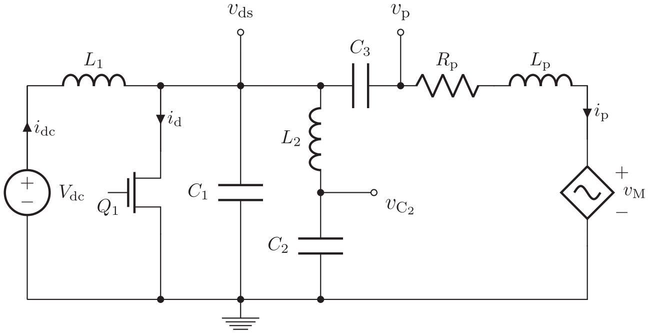

Fig. 2. Circuit diagram of the Class EF inverter with the load modelled as a dependent voltage source v_{M}.

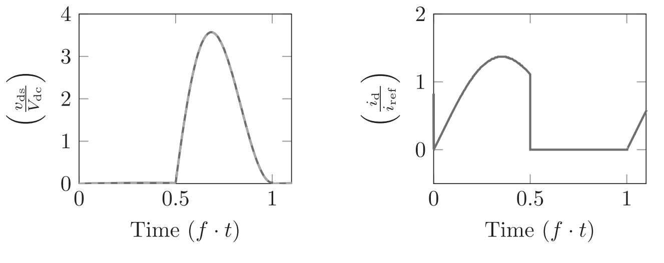

(a) (b)

Fig. 3. Theoretical waveforms of ZVS and ZDS of a Class E inverter with 50% duty cycle. (a) v_{ds}. (b) i_{d}.

by active power converters, these need to be frequency locked. Also, the harmonic content in i_{p} and i_{s}, and the losses associated with circulating currents at other frequencies are not considered in the phasor representation of v_{M}, however the receive coil at resonance (or close to resonance) will tend to filter out a substantial fraction of the harmonic content, depending on the loaded Q factor of the receiver, and therefore in the efficiency calculations these losses tend to be negligible.

B. Multiple Receivers and Coupled Objects

In an IPT system where the coil under test is coupled not only to one receiver, $\boldsymbol{v}_{\mathbf{M}}$ represents the superposition of the induced voltages produced by circulating currents in each of the receivers or other objects coupled to the coil under test

$$\boldsymbol{v}_{\mathbf{M}} = \boldsymbol{v}_{\mathbf{M_1}} + \boldsymbol{v}_{\mathbf{M_2}} + \cdots + \boldsymbol{v}_{\mathbf{M_N}} \tag{6}$$

with *N* being the number of coupled receivers or other objects in the IPT environment. This representation is not only useful to describe systems with more than one transmitter or receiver, but also systems in the presence of foreign objects. Interestingly, if there is knowledge of the loads coupled to the transmitter, from (6), the transmitter can be adapted to feed different loads and compensate for the voltages induced by metallic frames or other objects.

C. Challenges of Measuring the Induced Voltage in HF-IPT Coils

Probing v_{M} is not possible because it is distributed in the coil under test. It can be obtained, however, as a function of variables which can be measured. Intuitively, the most straightforward approach would be to measure the voltage between the terminals of the coil v_{p} in (1). This, however, requires i_{p} to be measured with accurate phase relative to $\boldsymbol{v}_{\mathbf{M}}$ in order to subtract $L_{\mathrm{p}}\frac{\mathrm{d}i_{\mathrm{p}}}{\mathrm{d}t}$, which is challenging at 6.78 or 13.56 MHz. In addition, probing v_{p} directly introduces a significant shunt-capacitance to the coil (e.g., the capacitance of our PMK voltage probes is 7.5 pF [31]), which is significant at these frequencies.

Our approach allows $\boldsymbol{v}_{\mathbf{M}}$ to be measured by probing solely the drain voltage (v_{ds}) of the transistor of a Class EF inverter (i.e., across the capacitance C_1 (see Fig. 2), where the capacitance of the probe can be easily accounted for), and avoiding the challenges and inconvenience of requiring differential measurements between two types of probe (current and voltage).

III. INVERTER AND THE LOAD RANGE

HF-IPT inverters are traditionally designed for a fixed resistive load [27], [32], [33]. For example, the theoretical component values of zero-voltage switching (ZVS) Class E inverters are found by solving for ZVS and zero derivative switching (ZDS)

$$\begin{aligned} v_{\mathrm{ds}}\Big|_{t=t_{\mathrm{on}}} &= 0 \\ \frac{\mathrm{d}v_{\mathrm{ds}}}{\mathrm{d}t}\Big|_{t=t_{\mathrm{on}}} &= 0 \end{aligned} \tag{7}$$

where t_{on} is the point in which the transistor is switched ON ($t = 1$ in Fig. 3). These conditions, assuming a constant coil inductance and constant capacitances, are satisfied only by one load resistance [32].

When ZVS and ZDS are not met, there are additional switching losses, and the degree at which these can be relaxed is determined by the thermal management of the board. In practice, the designer will have to allow a degree of tolerance to the conditions in (7) which can be written as

$$\begin{aligned} v_{\mathrm{ds}}\Big|_{t=t_{\mathrm{on}}} &< \mathrm{ZVS}_{\mathrm{boundary}} \\ \frac{\mathrm{d}v_{\mathrm{ds}}}{\mathrm{d}t}\Big|_{t=t_{\mathrm{on}}} &< \left|\mathrm{ZDS}_{\mathrm{boundary}}\right|. \end{aligned} \tag{8}$$

Determining boundaries as such is applicable not only to the conditions in (7), but also to other boundaries and design objectives such as the VA ratings of the switching devices, power dissipation, temperature, total harmonic distortion in the coil current, among others dictated by the application. For a given set of operating conditions (input voltage, frequency, and duty cycle), these design boundaries determine the range of admissible loads to the inverter. Moreover, the load boundaries are determined by the designer considering voltage, current, and temperature limits and other boundaries such as regulatory ones.

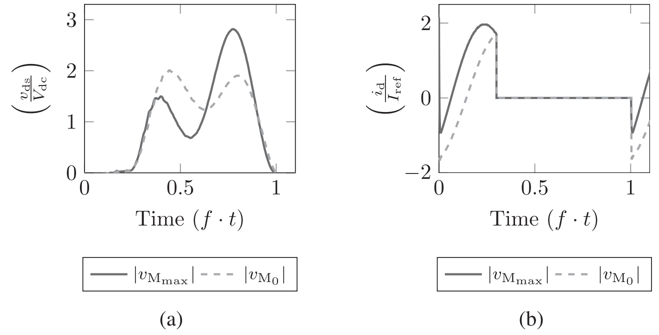

(a) (b)

Fig. 4. Theoretical waveforms of a load-independent Class EF inverter from zero to maximum load. (a) v_{ds}. (b) i_{d}.

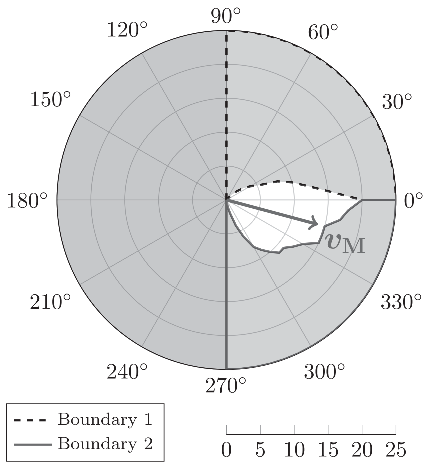

Fig. 5. Example phasor plot of $\boldsymbol{v}_{\mathrm{M}}$ considering two arbitrary boundaries to delimit its admissible range.

A. Class EF Inverter

The Class EF [27] (see Fig. 2) is a single-switch resonant inverter, which is commonly employed to drive transmit coils in HF-IPT systems. The principle of operation is similar to that of a Class E inverter but with the addition of an *LC* network (L_2, C_2 in Fig. 2) to decrease the peak voltage on v_{ds} and therefore achieve higher output power with a given set of transistor VA ratings. The additional freedoms due to the addition of L_2 and C_2 can be utilized to not only decrease the peak in v_{ds}, but also to modify the behavior of the switching waveforms.

The design of Class EF$_2$ and Class Φ_2 inverters, similarly to the Class E, also converge at one resistive load when the conditions of (7) are met [27], [34].

B. Load-Independent Class EF Inverter

The load-independent design of a Class EF inverter, introduced in [14], consists on a set of conditions that need to be met when sizing the passive components (see Fig. 2) so that v_{ds} converges to zero at turn ON independent of the magnitude of the load, as long as it is resistive, i.e., independent of the magnitude of $\boldsymbol{v}_{\mathrm{M}}$ as long as its phase is kept equal to that of i_{p}.

The load-independent feature is achieved when L_2, C_2 branch is tuned at a frequency other than the second or third harmonic of the switching frequency. The solutions which are found to be most practical are when the branch is tuned at 1.66 times the switching frequency. A list of the solutions, found with an exhaustive search algorithm, are given in [14, Table II]. The duty cycle of the driving signal is suggested at 30% in order to achieve the maximum power output capability of the switching device.

The waveforms of a theoretical solution for the load independent design are illustrated in Fig. 4. From these waveforms, it can be appreciated that v_{ds} at turn ON is zero from minimum to maximum $|\boldsymbol{v}_{\mathrm{M}}|$, however the ZDS is not met at any load value, and this is one of the compromises of this design which allows ZVS to be achieved independent of the amplitude of $\boldsymbol{v}_{\mathrm{M}}$.

C. Load Range of the Inverter

Once the inverter is operating in steady state, with a fixed driving signal (frequency and duty cycle) and a fixed input voltage, the inductively coupled objects are the only causes for change in the operating point. This allows the boundaries of the design to be expressed as a function of load. Fig. 5 is used as an illustration for the phasor plot of $\boldsymbol{v}_{\mathrm{M}}$ showing the limits at which the design boundaries are breached. A resistive load, for example, is described as a phasor at 0°, an inductive load (which reflects a capacitance) would have an angle of 270° and a capacitive load (which reflects an inductance) would have an angle of 90°. It should be noted that if the angle of $\boldsymbol{v}_{\mathrm{M}}$ is between 90° and 270°, the real part of $\boldsymbol{v}_{\mathrm{M}}$ is negative and the inverter would therefore be operating as a rectifier.

The results in Section IV are presented with respect to the amplitude and phase of $\boldsymbol{v}_{\mathrm{M}}$ using phasor plots as the one in Fig. 5.

IV. OBTAINING THE INDUCED VOLTAGE FROM THE DRAIN VOLTAGE WAVEFORMS

The magnitude and the phase of $\boldsymbol{v}_{\mathrm{M}}$ change the shape of v_{ds} of the transistor of a Class EF inverter in a distinctive manner [e.g., Fig. 4(a)]. We hypothesized that for a particular shape of v_{ds}, a single solution of $\boldsymbol{v}_{\mathrm{M}}$ exists. This hypothesis was tested by recording v_{ds} while stepping two variables: $|\boldsymbol{v}_{\mathrm{M}}|$ and θ_{s} relative to θ_{p}.

A. Design Methodology

An experimental rig was designed to test and record the waveforms of a Class EF inverter as a controlled load varies. The inverter is designed as follows: first, the coils are designed using an electromagnetic simulation tool (we use CST), and then they are constructed and measured (L and R) with an impedance analyzer at the frequency of operation. The capacitances and inductances of the topology (see Fig. 2) are then found using an in-house algorithm to comply with the load-independent equations derived for this topology in [14]. Finally, the inverter is tested with a tuned inductively coupled resistive load. Afterward, another board is populated using the same process, to be implemented as the synchronous rectifier. The same design can

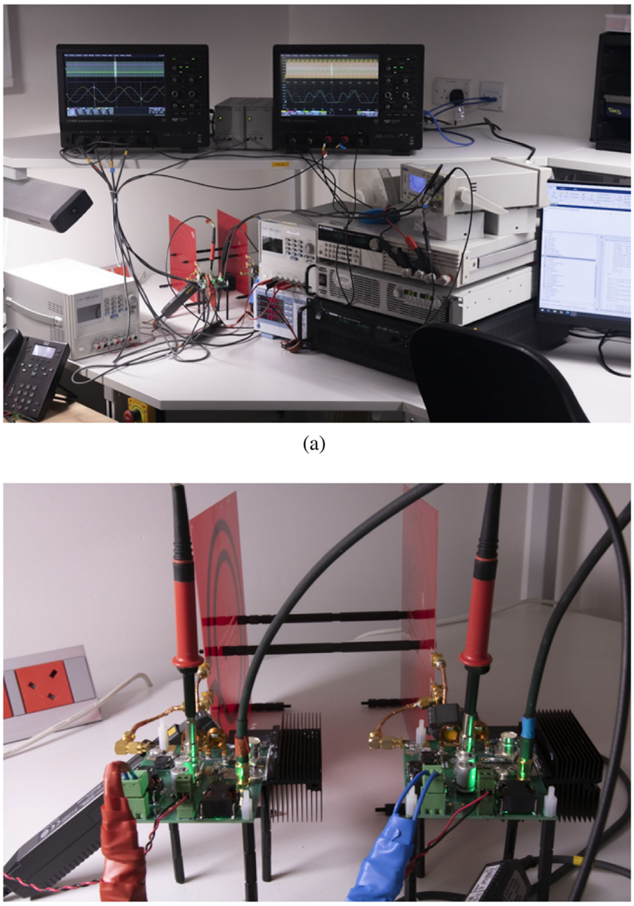

(a)

(b)

Fig. 6. Experimental setup. (a) Test setup and equipment. (b) IPT link and the 13.56 MHz coil drivers (inverter on the left and rectifier on the right).

be used in the inverter and rectifier due to the load-independent feature.

Once the inverter and rectifier boards are ready, the experiment to obtain the training data is designed as follows: the two coils are positioned at a fixed coupling, then the phase difference of the signals driving each board is stepped while checking the temperature of the transistors in the inverter and the rectifier to map out which points determine the thermal boundary of the operation. Additional data can be gathered by changing the current in the secondary coil, which can be done by changing the output voltage. Finally, within the couplings selected, the range in phase difference and the range in the output voltage, $\boldsymbol{v}_\mathrm{M}$ is stepped to record its corresponding v_ds. From these recorded waveforms, a pattern can then be found, using a regression algorithm (we use the Regression Learner toolbox from MATLAB) for the system to predict $\boldsymbol{v}_\mathrm{M}$ from the shape of v_ds.

B. Experimental Setup

A laboratory setup (see Fig. 6) was configured to record v_ds of the transistor of a Class EF inverter, experimentally, for a broad range of induced voltages from an inductively coupled test-load.

TABLE I
COMPONENTS VALUES FOR THE INVERTER AND RECTIFIER

Component	Value	Description
C_1 (pF)	100+C_oss	Vishay QUAD HIFREQ
C_2 (pF)	186	Vishay QUAD HIFREQ
C_3 (pF)	125	Vishay QUAD HIFREQ
L_1 (μH)	88	Wurth Elektronik WE-PD
L_2 (nH)	234	Coilcraft 2014VS
L_p & L_s (nH)	1181	IPT PCB coils
Q factor (Q_p & Q_s)	767	From [35]
Q_1	GS66504B (650 V, 15 A) GaN FET	

The setup consists of an IPT link comprised of two identical two-turn 210 mm (external diameter) printed-circuit-board coils, as designed in [28], each driven by identically tuned Class EF circuits, one as an inverter and the other as a synchronous rectifier. The component values can be found in Table I, considering the circuit schematic of Fig. 2.

Both Class EF circuits are driven by a signal from a two-channel signal generator (TG5011 A from TTI) at 13.56 MHz and a duty cycle of 30%, allowing the coil drivers to be synchronized. The transmit side was powered from a dc power supply (U8032 A by Keysight) and the receive side was connected to an electronic load (BK8512 from BK Precision). A power meter (WT332E by Yokogawa) was used to measure the input and output power and two synchronized four-channel oscilloscopes (HDO6104 A and HDO4034 A from Teledyne LeCroy) were used to measure: the driving signals, both v_ds (with PMK, PHV 1000 100:1 probes), and the current in both coils (with Keysight, N2783B active current probes) for verification.

C. Load Boundaries and the Operating Range for the Experiments

The input voltage of the inverter under test was kept constant at 80 V throughout the experiments. The output voltage of the rectifier was programmed with the electronic load to gradually step from 40 to 80 V, changing the amplitude of i_s. These measurements were repeated for the receiver at five locations corresponding to five values of k_ps ranging from 0.83% to 5.1%. The coil drivers were driven with a phase difference between -180° and 0°, since the power flow alternates (from the rectifier to the inverter) when the phase difference is positive for this coil configuration.

It was decided that for this experiment, the load range for the experiments would be determined by a single condition: that the GaN transistor, on either side of the link, was not to surpass a 70 °C threshold in a one-minute experiment (see Fig. 7), thus keeping a safety margin in the operation of the system. The temperature was measured using a Fluke Ti400 Thermal Imager. This boundary is specific to this experiment and the range of loads is dependent on the thermal performance of the board. For example, by including an additional fan, the range could be extended using the same boundary. We set the input and output voltages relatively low so that the thermal boundaries would not be reached that easily.

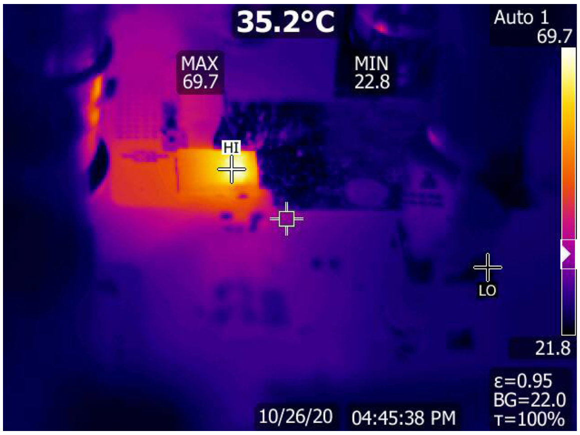

Fig. 7. Thermal image of the GaN transistor of the inverter under test close to 70 °C.

We ran initial experiments to determine the range in phase and the rectifier output voltage, which do not cross the thermal boundary for each k_{ps}, and the resulting boundary is illustrated in $\boldsymbol{v}_{\mathrm{M}}$ plots in Fig. 8. The experimental waveforms in Fig. 8 contain information of the switching performance of the inverter. For example, ZVS is achieved when powering the test load that produces a $\boldsymbol{v}_{\mathrm{M}}$ with a phase angle of zero [see Fig. 8(f)], but there is hard-switching when the test load induces a $\boldsymbol{v}_{\mathrm{M}}$ with a phase angle close to 90 °C [see Fig. 8(b)]. Also, notwithstanding that ZDS is not met in the load-independent designs, the derivative of v_{ds} at turn ON ($f \cdot t = 1$) is closer to zero when powering the test load 3 ($\boldsymbol{v}_{\mathrm{M}}$ with a phase angle of zero) than the other two.

The signal generator, the electronic load, and the oscilloscopes were connected to a computer to program automated steps in phase and amplitude, within the thermal boundary, and gather v_{ds} as a function of $\boldsymbol{v}_{\mathrm{M}}$. The phase between the signals was stepped in 2.5° intervals throughout the admissible range, and the amplitude was stepped by changing k_{ps} and the rectifier output voltage, in intervals corresponding to approximately 2 V in $|\boldsymbol{v}_{\mathrm{M}}|$.

D. Measurements, Data Gathering, and the SVM Model

For each tested $\boldsymbol{v}_{\mathrm{M}}$, 10 μs samples of the signals were recorded, however, in order to make the system more practical, the results presented herein use a fraction (slightly over 4 periods of the signal with 2.5 GS/s) of the data. The recorded signals were: i_{p}, i_{s}, and v_{ds}. i_{s} was measured to obtain $|\boldsymbol{v}_{\mathrm{M}}|$ from (2), since k_{ps} is known from previous works [28], and i_{p} was used as a phase reference for i_{s}, and therefore $\boldsymbol{v}_{\mathrm{M}}$. Other variables such as the inverter gate signal and the rectifier transistor drain voltage were also recorded but not required to predict $\boldsymbol{v}_{\mathrm{M}}$.

In total, data from 3424 combinations of k_{ps}, i_{s}, and $\theta_{\mathrm{s}} - \theta_{\mathrm{p}}$ were gathered to create the model using a linear SVM to predict $\boldsymbol{v}_{\mathrm{M}}$ from v_{ds}.

The model was obtained with a fivefold cross-validation (i.e., with five observations of 80% of the data and using the remaining 20% for validation). The resulting predictions are exemplified in Fig. 8, where different values of $\boldsymbol{v}_{\mathrm{M}}$ are predicted by observing v_{ds} of the inverter transistor.

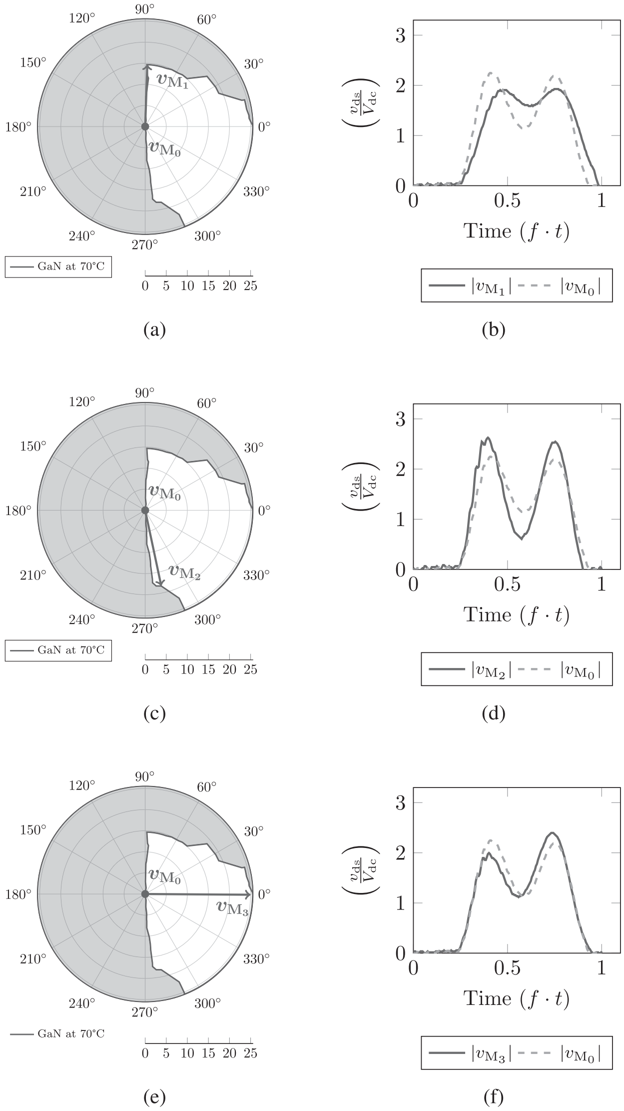

(a) (b)

(c) (d)

(e) (f)

Fig. 8. Experimental $\boldsymbol{v}_{\mathrm{M}}$ and v_{ds} plots for three test loads. (a) $\boldsymbol{v}_{\mathrm{M}}$ at test load 1. (b) v_{ds} at test load 1. (c) $\boldsymbol{v}_{\mathrm{M}}$ at test load 2. (d) v_{ds} at test load 2. (e) $\boldsymbol{v}_{\mathrm{M}}$ at test load 3. (f) v_{ds} at test load 3.

Once the model was formulated, a second set of data was gathered to further test the model. A randomized set of loads for three couplings out of the five used to create the model were tested. In order to test the accuracy of the model, an error vector ($\boldsymbol{Err}$) was formulated as

$$\boldsymbol{Err} = \boldsymbol{v}_{\mathrm{M}_{\mathrm{predicted}}} - \boldsymbol{v}_{\mathrm{M}_{\mathrm{measured}}} \tag{9}$$

where $\boldsymbol{v}_{\mathrm{M}_{\mathrm{measured}}}$ corresponds to the value of $\boldsymbol{v}_{\mathrm{M}}$ from (2), using the currents measurements and $\boldsymbol{v}_{\mathrm{M}_{\mathrm{predicted}}}$ represents the value of $\boldsymbol{v}_{\mathrm{M}}$ from the model using v_{ds}. The magnitude of the error vector ($|\boldsymbol{Err}|$) did not exceed 2 V for the entire test range, and the root-mean-square error (RMSE) was calculated at 0.51 V (1.0%). Fig. 9 shows a plot of the predicted $\boldsymbol{v}_{\mathrm{M}}$, and its associated $|\boldsymbol{Err}|$. The direction of $|\boldsymbol{Err}|$ is random, and consequently

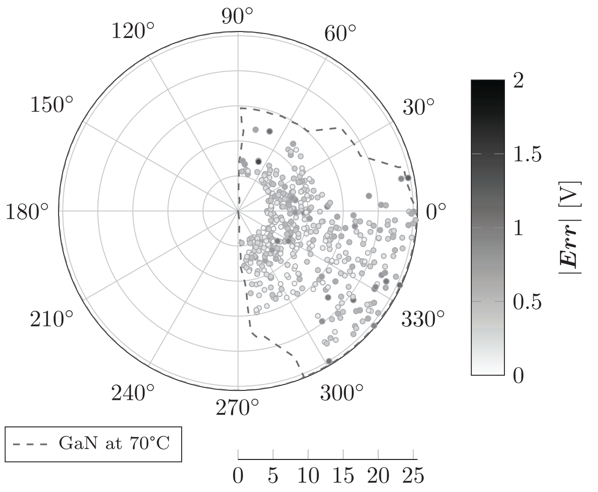

Fig. 9. Magnitude of the error with respect to $\boldsymbol{v}_\mathrm{M}$.

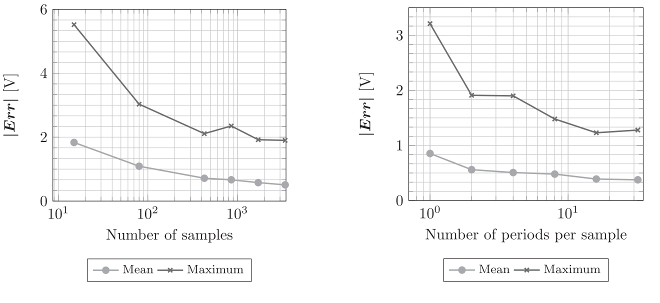

(a)

(b) v_ds

Fig. 10. Magnitude of the error with respect to the number of samples and the number of signal periods per sample.

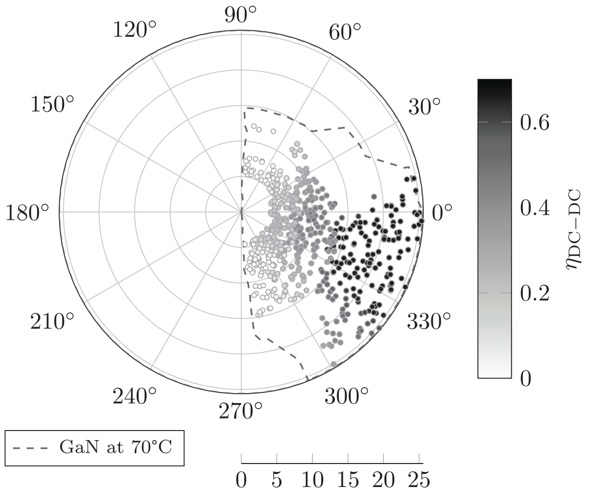

Fig. 11. DC–DC efficiency distribution with respect to $\boldsymbol{v}_\mathrm{M}$.

TABLE II
TEST LOAD CONFIGURATIONS AND ITS ASSOCIATED $\boldsymbol{v}_\mathrm{M}$

Case	Load Distance (k_ps)	Aluminium Sheet	$\boldsymbol{v}_\mathrm{M}$
1	no load	none	$0.3\ \mathrm{V}\angle{+87^\circ}$
2	no load	166 mm	$0.9\ \mathrm{V}\angle{-64^\circ}$
3	no load	101 mm	$14.4\ \mathrm{V}\angle{-88^\circ}$
4	274 mm (1.69 %)	none	$4.4\ \mathrm{V}\angle{+06^\circ}$
5	184 mm (4.13 %)	none	$24.0\ \mathrm{V}\angle{+06^\circ}$
6	184 mm (4.13 %)	119 mm from the transmitter	$25.2\ \mathrm{V}\angle{-17^\circ}$
7	184 mm (4.13 %)	119 mm from the receiver	$22.7\ \mathrm{V}\angle{+24^\circ}$

the average error in a large sample of measurements should converge to zero. An offset in this average would indicate that the model is not calibrated.

Alternative models were generated using a subsample of the data to determine the relationship between the $|\boldsymbol{Err}|$ and the number of samples. The lowest set of data used only 15 points, distributed throughout the range of $\boldsymbol{v}_\mathrm{M}$. Afterward, more data from randomized points were gradually introduced to create a more accurate model, finalizing in the model which uses all the data gathered. Fig. 10(a) illustrates the maximum error and the RMSE of the models using fewer data points. Also, alternative models using smaller (down to one period of the signal) and larger packages (up to 32 periods of the signal) of data were generated. The latter one shows the best performance with an RMSE of 0.376 V (0.8%). The results are illustrated in Fig. 10(b).

E. End-to-End Efficiency

The dc–dc efficiency of the system (measured with voltage and current probes at both dc ends of the system and corroborated with the power meter) is largely dictated by the real part of $\boldsymbol{v}_\mathrm{M}$, since it represents the resistive loading from the receiver to the transmitter. In the experiments, at the lower end of $\mathrm{Re}(\boldsymbol{v}_\mathrm{M})$, an additional power supply had to be connected in parallel to the electronic load since the power coming from the transmitter was not high enough to boost up the output voltage of the rectifier to the required value, indicating that the losses in the synchronous rectifier were greater than the power received from the transmitter. The power consumption of the inverter when unloaded was measured at 10.4 W. Therefore, if the current in the coil is 5.5 A, a $\boldsymbol{v}_\mathrm{M}$ of 3.78 V in $\mathrm{Re}(\boldsymbol{v}_\mathrm{M})$ would be required to bring the output voltage up to 80 V. It is therefore expected that any case in which $\mathrm{Re}(\boldsymbol{v}_\mathrm{M})$ is lower than 3.78 V would have an efficiency of zero.

The distribution of the end-to-end efficiency with respect to $\boldsymbol{v}_\mathrm{M}$ is illustrated in Fig. 11. The highest efficiency of 68.1% was achieved at $\boldsymbol{v}_\mathrm{M} = 25.4\ \mathrm{V}\ \angle{-2.9^\circ}$, and the lowest efficiency was zero at various points, where $\mathrm{Re}(\boldsymbol{v}_\mathrm{M})$ was close to zero (i.e., the additional power supply was required to bring up the output voltage of the rectifier).

F. Characterization of a Passive Load and a Metallic Object

Further testing of the model was conducted by removing the receiver with a synchronous rectifier and placing a passive test load (an *RLC* circuit tuned at 13.56 MHz) and an aluminum sheet with the same dimensions as the coils PCB (230 mm × 230 mm) at different positions close to the transmit coil. The configurations tested are specified in Table II, and the results

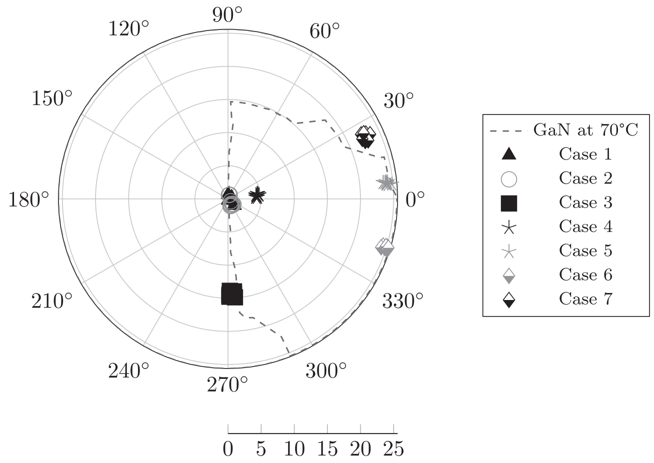

Fig. 12. Predicted $\boldsymbol{v}_{\mathrm{M}}$ for different configurations of the link with passive receivers.

of ten $\boldsymbol{v}_{\mathrm{M}}$ estimations of each of the seven configurations are plotted in Fig. 12. We included cases with and without the tuned load, and with and without a metallic object. The position of the load was tested at very low coupling (1.69%) and the coupling at which the induced voltage on the primary reached the boundary (see case 5 in Table II). The proximity of the metallic object was also selected based on the boundaries. It should be noted that the effect produced by a metallic object depends on its size, shape, material, and position with respect to the coils, and the metallic object presented here has the sole purpose of exemplifying how the presence of a metallic object might affect $\boldsymbol{v}_{\mathrm{M}}$.

The metallic object (cases 2 and 3), as expected, reflects a reactive load ($\boldsymbol{v}_{\mathrm{M}} = 14.4\ \mathrm{V}\ \underline{/-88^{\circ}}$ in case 3), and it had to be placed closer to the coil than the tuned load for the effect to be noticeable.

The resistive load, which was tuned with a E4990A impedance analyzer from Keysight, loads the inverter mostly on the real axis ($\boldsymbol{v}_{\mathrm{M}} = 24.0\ \mathrm{V}\ \underline{/+06^{\circ}}$ in case 5), and the addition of the aluminum sheet (cases 6 and 7) shows how the effect in both cases decreases the load on the real axis (it decreases the mutual inductance of the coils) and how the angle shifts to different directions depending on which of the coils is most affected by the metallic sheet.

V. CONCLUSION

Knowledge of the voltage induced from the load to the transmitter is useful for various reasons. First, it can be used to determine whether the operating point of the inverter is within the design limits. For example, in our experimental work, we determined, as an operation boundary, that the transistors on both boards should operate without exceeding a thermal threshold, and this gives a range of operation with regards to the inductively coupled loads. Second, it provides information about the types of loads (resistive, capacitive, inductive), which are mutually coupled to the transmitter allowing the system to detect anomalies such as foreign objects within the energized zone. In the experiments, for example, when a metallic sheet was placed closely to the transmit coil, the angle of $\boldsymbol{v}_{\mathrm{M}}$ indicated that the transmitter was driving an equivalent circuit, which does not correspond to solely a tuned reflecting a resistance, but rather there was also an inductive load reflecting a capacitance.

Our approach to estimate $\boldsymbol{v}_{\mathrm{M}}$, which cannot be probed directly, is to solely observe how the drain-voltage waveform of the Class EF inverter (which is convenient to probe) changes with load. From this, we demonstrate, experimentally, that $\boldsymbol{v}_{\mathrm{M}}$ can be predicted with a maximum error magnitude lower than 1.5V (3%) from v_{ds} alone, once its shape has been characterized with respect to known loads.

REFERENCES

[1] A. Kurs, A. Karalis, R. Moffatt, J. D. Joannopoulos, P. Fisher, and M. Soljačić, "Wireless power transfer via strongly coupled magnetic resonances," *Science*, vol. 317, no. 5834, pp. 83–86, 2007.

[2] S. Y. R. Hui, W. Zhong, and C. K. Lee, "A critical review of recent progress in mid-range wireless power transfer," *IEEE Trans. Power Electron.*, vol. 29, no. 9, pp. 4500–4511, Sep. 2014.

[3] M. Pinuela, D. C. Yates, S. Lucyszyn, and P. D. Mitcheson, "Maximizing DC-to-load efficiency for inductive power transfer," *IEEE Trans. Power Electron.*, vol. 28, no. 5, pp. 2437–2447, May 2013.

[4] J. Choi, D. Tsukiyama, Y. Tsuruda, and J. Rivas, "13.56 MHz 1.3 kW resonant converter with GaN FET for wireless power transfer," in *Proc. IEEE Wireless Power Transfer Conf.*, May 2015, pp. 1–4.

[5] M. Liu, S. Liu, and C. Ma, "A high-efficiency/output power and low-noise megahertz wireless power transfer system over a wide range of mutual inductance," *IEEE Trans. Microw. Theory Techn.*, vol. 65, no. 11, pp. 4317–4325, Nov. 2017.

[6] A. L. F. Stein, P. A. Kyaw, and C. R. Sullivan, "Wireless power transfer utilizing a high-*q* self-resonant structure," *IEEE Trans. Power Electron.*, vol. 34, no. 7, pp. 6722–6735, Jul. 2019.

[7] G. Zulauf and J. M. Rivas Davila, "Single-turn air-core coils for high-frequency inductive wireless power transfer," *IEEE Trans. Power Electron.*, vol. 35, no. 3, pp. 2917–2932, Mar. 2020.

[8] J. M. Arteaga, S. Aldhaher, G. Kkelis, D. C. Yates, and P. D. Mitcheson, "Multi-MHz IPT systems for variable coupling," *IEEE Trans. Power Electron.*, vol. 33, no. 9, pp. 7744–7758, Sep. 2018.

[9] J. Choi, Y. Ooue, N. Furukawa, and J. Rivas, "Designing a 40.68 MHz power-combining resonant inverter with eGaN FETs for plasma generation," in *Proc. IEEE Energy Convers. Congr. Expo.*, 2018, pp. 1322–1327.

[10] J. M. Arteaga, S. Aldhaher, G. Kkelis, C. Kwan, D. C. Yates, and P. D. Mitcheson, "Dynamic capabilities of multi-MHz inductive power transfer systems demonstrated with batteryless drones," *IEEE Trans. Power Electron.*, vol. 34, no. 6, pp. 5093–5104, Jun. 2019.

[11] C. H. Kwan, J. M. Arteaga, D. C. Yates, and P. D. Mitcheson, "Design and construction of a 100 w wireless charger for an e-scooter at 6.78 MHz," in *Proc. IEEE PELS Workshop Emerg. Technol., Wireless Power Transfer*, 2019, pp. 186–190.

[12] L. Lan, C. H. Kwan, J. M. Arteaga, D. C. Yates, and P. D. Mitcheson, "A 100 W 6.78 MHz inductive power transfer system for drones," in *Proc. Eur. Conf. Antennas Propag.*, 2020, pp. 1–4.

[13] N. Pucci, C. H. Kwan, D. C. Yates, and P. D. Mitcheson, "Multi-megahertz IPT systems for biomedical devices applications," in *Proc. Int. Conf. Micro Nanotechnol. Power Gener. Energy Convers. Appl.*, 2019, pp. 1–7.

[14] S. Aldhaher, D. C. Yates, and P. D. Mitcheson, "Load-independent class E/EF inverters and rectifiers for MHz-switching applications," *IEEE Trans. Power Electron.*, vol. 33, no. 10, pp. 8270–8287, Oct. 2018.

[15] W. D. Braun and D. J. Perreault, "A high-frequency inverter for variable-load operation," *IEEE Trans. Emerg. Sel. Topics Power Electron.*, vol. 7, no. 2, pp. 706–721, Jun. 2019.

[16] A. Kumar, S. Sinha, and K. K. Afridi, "A high-frequency inverter architecture for providing variable compensation in wireless power transfer systems," in *Proc. IEEE Appl. Power Electron. Conf. Expo.*, 2018, pp. 3154–3159.

[17] Y. Han, O. Leitermann, D. A. Jackson, J. M. Rivas, and D. J. Perreault, "Resistance compression networks for radio-frequency power conversion," *IEEE Trans. Power Electron.*, vol. 22, no. 1, pp. 41–53, Jan. 2007.

[18] G. Kkelis, D. C. Yates, and P. D. Mitcheson, “Class-E half-wave zero dv/dt rectifiers for inductive power transfer,” *IEEE Trans. Power Electron.*, vol. 32, no. 11, pp. 8322–8337, Nov. 2017.

[19] K. Li, S. Tan, and R. S. Y. Hui, “Single-switch-regulated resonant WPT receiver,” *IEEE Trans. Power Electron.*, vol. 34, no. 11, pp. 10 386–10 391, Nov. 2019.

[20] L. Gu, G. Zulauf, Z. Zhang, S. Chakraborty, and J. Rivas-Davila, “Push-pull class ϕ_2 rf power amplifier,” *IEEE Trans. Power Electron.*, vol. 35, no. 10, pp. 10 515–10 531, Oct. 2020.

[21] G. Covic and J. T. Boys, “Modern trends in inductive power transfer for transportation applications,” *IEEE Trans. Emerg. Sel. Topics Power Electron.*, vol. 1, no. 1, pp. 28–41, Mar. 2013.

[22] S. Li and C. C. Mi, “Wireless power transfer for electric vehicle applications,” *IEEE Trans. Emerg. Sel. Topics Power Electron.*, vol. 3, no. 1, pp. 4–17, Mar. 2015.

[23] A. Zaheer, M. Neath, H. Z. Z. Beh, and G. A. Covic, “A dynamic EV charging system for slow moving traffic applications,” *IEEE Trans. Transp. Electrific.*, vol. 3, no. 2, pp. 354–369, Jun. 2017.

[24] D. Patil, M. K. McDonough, J. M. Miller, B. Fahimi, and P. T. Balsara, “Wireless power transfer for vehicular applications: Overview and challenges,” *IEEE Trans. Transp. Electrific.*, vol. 4, no. 1, pp. 3–37, Mar. 2018.

[25] Y. Zhang, Z. Yan, J. Zhu, S. Li, and C. Mi, “A review of foreign object detection (FOD) for inductive power transfer systems,”*eTransportation*, vol. 1, 2019, Art. no. 100002.

[26] D. J. Thrimawithana, U. K. Madawala, and M. Neath, “A synchronization technique for bidirectional ipt systems,” *IEEE Trans. Ind. Electron.*, vol. 60, no. 1, pp. 301–309, Jan. 2013.

[27] Z. Kaczmarczyk, “High-efficiency class e, EF_2, and E/F_3 inverters,” *IEEE Trans. Ind. Electron.*, vol. 53, no. 5, pp. 1584–1593, Oct. 2006.

[28] J. M. Arteaga, L. Lan, S. Aldhaher, G. Kkelis, D. C. Yates, and P. D. Mitcheson, “A multi-MHz IPT-link developed for load characterisation at highly variable coupling factor,” in *Proc. IEEE Wireless Power Transfer Conf.*, Jun. 2018, pp. 1–4.

[29] L. Lan, J. M. Arteaga, D. C. Yates, and P. D. Mitcheson, “A reflected impedance estimation technique for inductive power transfer,” in *Proc. IEEE PELS Workshop Emerg. Technol., Wireless Power*, Jun. 2019, pp. 1–4.

[30] J. M. Arteaga, L. Lan, C. H. Kwan, D. C. Yates, and P. D. Mitcheson, “Characterisation of high frequency inductive power transfer receivers using pattern recognition on the transmit side waveforms,” in *Proc. IEEE Appl. Power Electron. Conf. Expo.*, 2020, pp. 825–831.

[31] *High Voltage Passive Probe Datasheet, PMK, 2020*, Rev. 10.2020.

[32] M. K. Kazimierczuk and D. Czarkowski, *Resonant Power Converters*. Hoboken, NJ, USA: Wiley, 2012.

[33] N. O. Sokal and A. D. Sokal, “Class E-A new class of high-efficiency tuned single-ended switching power amplifiers,” *IEEE J. Solid-State Circuits*, vol. 10, no. 3, pp. 168–176, Jun. 1975.

[34] R. C. N. Pilawa-Podgurski, A. D. Sagneri, J. M. Rivas, D. I. Anderson, and D. J. Perreault, “Very-high-frequency resonant boost converters,” *IEEE Trans. Power Electron.*, vol. 24, no. 6, pp. 1654–1665, Jun. 2009.

[35] E. Skountzos, J. M. Arteaga, E. Hadjittofis, D. C. Yates, K. L. Sedransk Campbell, and P. D. Mitcheson, “A 13.56 MHz inductive power transfer system operating with corroded coils,” in *Proc. IEEE PELS Workshop Emerg. Technol., Wireless Power Transfer*, 2019, pp. 335–340.

Juan M. Arteaga (Member, IEEE) received the B.Sc. and Licentiate (hons.) degrees in electrical engineering from the University of Costa Rica, San Pedro, Costa Rica, in 2008 and 2010, respectively, the M.Sc. degree in micro and nanoelectronics from the Autonomous University of Barcelona, Bellaterra, Spain, in 2011, and the Ph.D. degree in electrical and electronic engineering from Imperial College London, London, U.K. in 2020.

His doctoral research focused on the integration of high-frequency inductive power transfer systems into applications. He is currently a Research Associate with the Control and Power Research Group, Department of Electrical and Electronic Engineering, Imperial College London, London, U.K. His research interests include power electronics, high-frequency resonant converters, and wireless power transfer.

Dr. Arteaga received the 2019 IEEE Transactions on Power Electronics Second Prize Paper Award and the Eryl Cadwallader Davies Prize for his Ph.D. thesis.

Nunzio Pucci (Member, IEEE) received the M.Eng. degree in electrical and electronic engineering in 2019 from Imperial College London, London, U.K., where he is currently working toward the Ph.D. degree.

His research interests include power electronics, resonant converters, wireless power transfer, custom instrumentation, and machine learning.

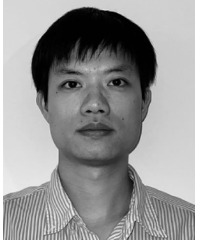

Lingxin Lan received the B.Eng. degree in electrical and electronic engineering in 2017 from Imperial College London, London, U.K., where he is currently working toward the Ph.D. degree in electrical and electronic engineering.

His research interests include the safety system design and integration of wireless power transfer and applied machine learning.

Paul D. Mitcheson (Senior Member, IEEE) received the M.Eng. degree in electrical and electronic engineering and the Ph.D. degree in micropower motion based energy harvesting for wireless sensor networks from Imperial College London, London, U.K., in 2001 and 2005, respectively.

He is currently a Professor in Electrical Energy Conversion with the Control and Power Research Group, Electrical and Electronic Engineering Department, Imperial College London. His research interests include energy harvesting, power electronics, and wireless power transfer to provide power to applications in circumstances where batteries and cables are not suitable. His research has been supported by the European Commission, Engineering and Physical Sciences Research Council, and several companies.

Prof. Mitcheson is a fellow of the Higher Education Academy and is on the Executive Committee of the U.K. Power Electronics Centre. He was the General Co-Chair of IEEE Wireless Power Week in 2019 in London, U.K.